Preferred orientation of calcium aluminosilicate hydrate compacts: Implications for creep and indentation

Jiaqi Li [*], Wenxin Zhang, Paulo J.M. Monteiro

Department of Civil and Environmental Engineering, University of California, Berkeley, United States

ARTICLE INFO

ABSTRACT

Nano/micro-indentation has been extensively used to examine elastic properties and creep of cement-based materials. However, there have been inconsistencies in the measured elastic moduli and debate on the creep mechanism of calcium (alumino) silicate hydrates (C-(A-)S-H). To bring new insights, we examined the deviatoric stress-induced preferred orientation of calcium aluminosilicate hydrate (C-A-S-H), portlandite, and ettringite compacts, using synchrotron-based X-ray diffraction. Intense preferred orientations were observed in C-A-S-H compacts, and the c-axis of unit cells is highly aligned with the compression direction; weaker c-axis related fiber-type texture formed in portlandite and ettringite. Higher humidity, greater compacting pressure, and/or increased duration of the pressure intensified the C-A-S-H preferred orientation, which is facilitated by gel-pore water lubrication. This pressure-induced time-dependent preferential re-orientation of crystallites can contribute to the creep of cement-based materials, and it may cause overrepresentation of the soft c-axis of C-(A-)S-H unit-cell in nanoindentation experiments and underestimation of Young's modulus.

1. Introduction

Elastic constants (e.g., Young's modulus, bulk modulus, and Poisson's ratio) of hydration products are essential inputs for micromechanics modeling of mechanical proprieties of cement-based materials [1]. As calcium (alumino) silicate hydrate (C-(A-)S-H) is the major hydration product and the primary binding phase in Portland cement, measurements of the elastic constants of C-(A-)S-H are of great interest.

Except for C-(A-)S-H, elastic constants of single-crystal phases, e.g., ettringite [2] and portlandite [3], can be readily measured by Brillouin spectroscopy. C-(A-)S-H is porous, poorly crystalline, and structurally variable [4–5] (see Fig. 1). C-(A-)S-H is structurally similar to a defective (Al-)tobermorite: at high Ca/Si molar ratios, C-S-H has short silicate chains with bridging Ca; at low Ca/Si molar ratios, C-S-H has long silicate chains with silica-occupied bridging sites, and cross-linked bridging sites are not commonly found or validated even at elevated equilibrium temperature (e.g., 80 °C) [6–8]; C-A-S-H has longer aluminosilicate chains with aluminate tetrahedra incorporated at bridging sites, at room temperature, the bridging sites are non-cross-linked and the Al incorporated bridging sites are cross-linked at elevated temperature [8]; and the interlayer spacing of C-(A-)S-H is sensitive to drying conditions or

relative humidity [9]. Thus, determining the elastic constants of C-(A-)S-H is challenging. Young's modulus of C-(A-)S-H in hardened cement pastes is often obtained from micro-/nano-indentation or atomic force microscopy. The indentations are sensitive to many factors (e.g., surface roughness [10–11], indentation depth [12], heterogeneity of the cement paste microstructure [13]). The values of the C-(A-)S-Hs moduli were obtained from deconvolution of probability distribution function and were often highly discrepant (see Table 1). The Young's modulus calcium silicate hydrate (C-S-H) obtained from indentation techniques often ranges from 15 GPa to 45 GPa [13–14], which overlaps with the Young's moduli of ettringite, 25 ± 2 GPa [2], and portlandite, 42.8 ± 0.8 GPa [3]. Thus, the data processing of indentation heavily relies on the assumption of the Young's moduli of C-S-H with different densities and intermixed impurities [15]. A recent nanoindentation study [13], which coupled with qualitative energy-dispersive spectroscopy, provided the micro-chemo-mechanical information of different phases of cement pastes and identified phase pure inner product C-S-H at submicron scale from phase assemblages. The study suggested that Young's modulus of inner product C-S-H is 28 GPa while probing outer product C-S-H is challenging as outer product is intermixed with other phases, e. g., portlandite. The micro-chemo-mechanical method has been applied to probe the inner product of blended cement, and the variation of

---

Young's modulus of the inner product C-(A-)S-H is only ~10% [16] at the same water-to-binder ratio.

There is a burgeoning interest in exploring the Young's modulus of synthetic phase-pure C-(A-)S-H which eliminates the influence of impurities on the indentation results. In the nanoindentation studies of pure C-S-Hs, the influence of Ca/Si ratios [17], polymer incorporation [18], and aluminum incorporation [19] on Young's modulus can be examined after compacting powder samples. However, the results obtained from indentation studies were sensitive to the homogeneity in the material. Multimodal distributions of Young's modulus of synthetic C-S-H compacts were reported in [20]. With careful sample preparations, Hay et al. [21] suggested that compacts of synthetic C-S-H and calcium alumino silicate hydrate (C-A-S-H) have unimodal distribution. Recent studies [21–22] further demonstrated that the indentation results of C-S-H and C-A-S-H compacts are sensitive to compacting stress, holding time, conditioning humidity, compact porosity, and testing parameters.

The bulk modulus of C-(A-)S-H can be reliably measured at the molecular-to-nano scale using high-pressure X-ray diffraction (HP-XRD). The pressure-transmitting medium, e.g., silicone oil, can fill the gel pores of C-(A-)S-H, thus eliminating the influences of gel pores on the mechanical properties. The measured mechanical properties of C-(A-)S-H in recent HP-XRD studies under this hydrostatic condition are consistent and are correlated to the influences of the unit cell structure of C-(A-)S-H [23–24]. Young's moduli of C-(A-)S-H at this pore-free scale are converted to be 81–107 GPa, which are significantly larger than those obtained from indentation. The modulus results obtained from different sample preparations and characterization techniques are summarized in Table 1. These techniques have different length scales of probed interactive volumes of samples and varying resolution. HP-XRD can probe the mechanical properties of C-(A-)S-H at sub-nanometer resolution of bulk samples with volume of tens of μm^3. The indentation depth of cement-based samples in microindentation studies can be a few microns, e.g., 15 μm in [22], and the estimated probed interactive volume can be hundreds of μm^3. For probing phase-pure C-(A-)S-H by nanoindentation, the suggested maximum indentation depth is 100–300 nm [25], and the probed volume size is a few μm^3, which is much larger than the C-S-H building blocks, i.e., 4–5 nm [26]. As summarized in [13], Young's modulus measurement of C-(A-)S-H with nanoindentation is also sensitive to water-to-cement ratios of cement-based materials. It is well known that ordinary Portland cement pastes with higher water content have higher capillary porosity [27]. The water-to-cement ratio dependent capillary porosity, particularly the fine capillaries, e.g., pore size <100 nm, may affect the results of C-(A-)S-H measured by micro- and nano-indentation as the probed interactive volumes of the techniques include the fine capillary pores.

C-(A-)S-H compacts are also useful for the studies of creep, which influences the service life of Portland cement-based materials [36] and also alkali-activated materials [37]. The creep mechanism of these materials is not fully understood. Different creep theories have been proposed [38–43]. The creep of C-(A-)S-H compacts have been studied using indentation techniques [19,22,44] and the experimental results showed that the measured creep moduli were sensitive to the porosity of C-(A-)S-H compacts. Our recent HP-XRD study unveiled the preferred orientation of C-A-S-H nanocrystals exposed to deviatoric stress in the absence of pressure-transmitting medium [35]. The findings indicate that the nanocrystals in C-(A-)S-H compacts can be reoriented after compaction, and the results from indentation studies may not represent the real microscopic and macroscopic properties of bulk C-(A-)S-H. Moreover, the role of water or relative humidity, a critical factor of cement/concrete creep [36,45–46], in the development of preferred orientation of C-(A-)S-H was not experimentally validated in our previous study [35].

In this study, the preferred orientation of C-A-S-H powder after compaction is studied using synchrotron-radiation-based X-ray diffraction. The influences of compacting pressure, holding time, and humidity on the orientation of C-A-S-H nanocrystals are evaluated. Additionally, the preferred orientation of portlandite (Ca(OH)$_2$) and ettringite (Ca$_6$Al$_2$(SO$_4$)$_3$(OH)$_{12}$·26H$_2$O) powder after compaction is also studied for a comparison with C-A-S-H. These investigations can explain the limitations of the sample preparation in existing literature and the technical limitations of nanoindentation.

2. Materials and methods

2.1. Materials

Cross-linked C-A-S-H with a bulk Ca/(Al + Si) molar ratio of 1 and a bulk Al/(Al + Si) molar ratio of 0.1 were synthesized according to a modification of the protocol in [8]. Stoichiometric amounts of CaO, silica fume (Aerosil 200, Evonik) and CaO·Al$_2$O$_3$ (Mineral Research Processing) were mixed with deionized water at a water-to-solid mass ratio of 45 in an N$_2$-filled glove box at 25 °C. The slurry was then cured in a water-bath at 80 °C in a 250 mL Teflon bottle for 91 days. The C-A-S-H slurry was vacuum-filtered using 450 nm nylon filters in an N$_2$-filled glove box. The solid remnant solid was firstly dried in a N$_2$-filled desiccator for 14 days in the presence of NaOH pellets, and then freeze-dried for four days. Two sets of C-A-S-H samples were prepared: 1) The dry C-A-S-H sample used in the experiment was taken directly from the freeze-dried C-A-S-H and sealed until analysis; 2) the wet C-A-S-H sample was obtained by further equilibrating the freeze-dried C-A-S-H in an environment with deionized water for seven days at relative humidity (RH) of 100%. Freeze-drying of cementitious materials for four days is relatively intense and is efficient to remove the water in gel pores of C-A-S-H and to avoid the fast carbonation of ultrafine C-A-S-H powder. This harsh drying procedure is important as our interest is to study to influence of water, particularly water in pores (e.g., gel pores), on the preferred orientation of C-A-S-H. Although harsh freeze-drying alters the microstructure of hardened cement pastes [47], the microstructure (e.g.,
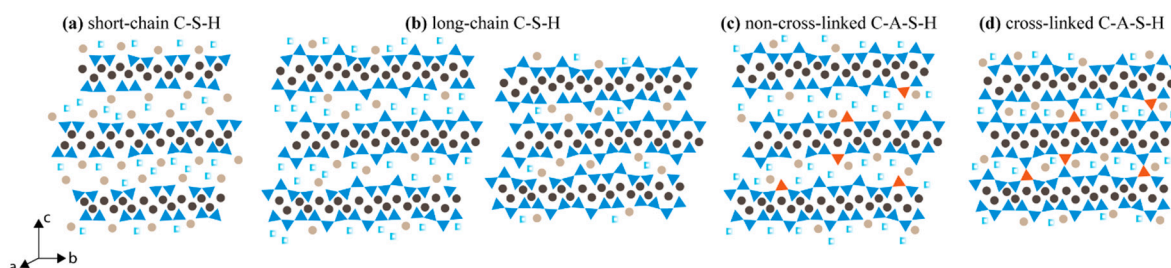
Fig. 1. Schematic diagram of C-(A-)S-H. (a) short-chain C-S-H at high Ca/Si ratios; (b) long-chain C-S-H at low Ca/Si ratios, left: at high relative humidity (RH), right: at low relative humidity; (c) non-cross-linked calcium alumino silicate hydrate (C-A-S-H) at room temperature; (d) cross-linked C-A-S-H at elevated temperature. Blue and orange triangles represent SiO$_4$ and AlO$_4$ tetrahedra, respectively; dark and light brown circles represent intralayer and interlayer Ca, respectively; and light blue squares represent water molecules. Two pairs of silicate tetrahedra are connected with one bridging aluminate/silicate tetrahedron or bridging Ca. (For interpretation of the references to color in this figure legend, the reader is referred to the web version of this article.)

capillary pore size) of the fine powder sample is irrelevant to the present study and is out of our scope. A comparative study has shown that a freeze-dried cement paste has the minimal degree of carbonation [48]. Freeze-drying for ~7 days is commonly used in the sample preparation of synthetic C-(A-)S-H fine powder samples [7–8,49]. Our previous thermogravimetric study has shown that the free pore water content of the freeze-dried C-A-S-H fine powder is <4%, while the C-A-S-H fine powder equilibrated at 75% RH has ~10% of this water. For more details, see [21].

Portlandite fine powder with 99 + % purity was acquired from FisherScientific. Ettringite powder was obtained from Mineral Research Processing. Portlandite and ettringite were sealed until analysis to avoid carbonation or dehydration.

2.2. Compact preparation

C-A-S-H, portlandite, or ettringite powder was loaded using a dry pellet pressing die (diameter 3.175 mm, MTI). A vertical force was applied to exert a maximum compressive pressure of 200 or 500 MPa on the sample; the maximum loading was either instantaneous or held for 300 s. Then the die was unloaded immediately. The final products after compaction were compacts with ~1 mm thickness. The compacts were tested immediately after compaction.

2.3. Synchrotron-based X-ray diffraction (XRD)

XRD experiment was conducted at the beamline 12.2.2 of the Advanced Light Source at the Lawrence Berkeley National Laboratory. The compact was placed horizontally on the sample holder. The monochromatic incident X-ray, with a beam size of 30 μm, was centered to the compact. 2D diffraction image was recorded with a MAR345 area detector at a 330.5-mm distance from the sample (Fig. 2). The wavelength of the synchrotron X-ray was 0.4973 Å; the exposure time was 60 s for each sample. The beam-sample interaction volume is about 30 μm^3. XRD of reference samples (in absence of any compression or compaction; in the form of loose powder in a glass capillary) were also collected for comparison.

Fig. 2. Schematic of the XRD experiment. The direction of the x-axis is parallel to the compressive load and coincides with the 0°-azimuth ($\eta = 0°$) as defined in the texture analysis.

2.4. Texture analysis

The texture quantification via Rietveld refinement was performed on the MAUD software [50]. Note that, the term "texture" here refers to the preferred orientation of deformed polycrystalline materials, not the morphology or microstructure of materials often used in cement chemistry. The input phase for the nanocrystalline C-A-S-H samples is the monoclinic 11 Å tobermorite (Merlino) of space group B11m, with a = 6.732 Å, b = 7.369 Å, c = 22.38 Å, and γ = 123.18° [51]; the portlandite phase is of space group P-3 m 1, with a = 3.585 Å and c = 4.895 Å; the ettringite phase is of space group P31c, with a = 11.234 Å and c = 21.474 Å. Different model structures of tobermorite or C-S-H can be used to fit the nanostructure of C-A-S-H [52–54]. Our previous study has shown that the use of different model structures has a negligible influence on the refinement of lattice parameters of nanocrystalline C-A-S-H [23], which is known to have a defective tobermorite-like structure. And Merlino's tobermorite structure [55] is commonly used to refine the structure of nanocrystalline C-(A-)S-H. The raw 2D diffraction image

Table 1
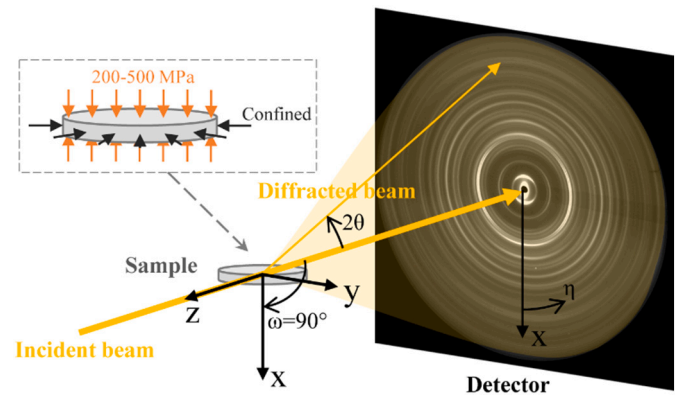Modulus results of C-(A-)S-H using different characterization techniques.

Samples	Ca/(Al + Si)	Al/Si	Method	Young's modulus (GPa)	Bulk modulus (GPa)	Probed volume size/resolution
Concrete	LD[a]		Nanoindentation	18.6 [28]		Submicron[d]
	HD[a]			32.2 [28]		
Cement pastes	LD		Nanoindentation	23.4 [29], 18.2 [25], 33.4 [30], 32.7 [30], 28.0 [30], 29.7 [30], 31.6 [30], 24.2 [31], 23.0 [32], 18.1 [33], 21.7 [34]		Submicron to ~1 μm[d]
	HD			31.4 [29], 29.1 [25], 46.9 [30], 40.5 [30], 44.0 [30], 36.1 [30], 46.6 [30], 28.2 [31], 25.7 [32], 30.0 [33], 29.4 [34]		
Synthetic C-S-H compact	Mixed		Microindentation	41.7 [22]		15 μm[d]
Synthetic C-S-H compact	0.7		Nanoindentation	24.1–27.0 [17]		~1 μm[d]
	2.1			15.8–20.3 [17]		
Synthetic C-S-H compact	1.2		Nanoindentation	4–48 [20]		Unknown[d]
Synthetic C-S-H compact	1.0		Nanoindentation	5–19 [21]		Submicron to ~1 μm[d]
Synthetic C-A-S-H compact	1.0	0.1	Nanoindentation	5.5–7.9 [21]		Submicron to ~1 μm[d]
Synthetic C-S-H powder	0.8		High-pressure X-ray diffraction	80.5[b]	58.3 [24]	Unit cell scale with probed volume of ~30 μm^3
	1.0			95.8[b]	69.4 [24]	
	1.3			106.8[b]	77.4 [24]	
Synthetic C-A-S-H powder	0.94	0.05		92.2[c]	64 [24]	
	0.87	0.05		102.2[c]	71 [24]	

[a] Ca/Si ratio unknown. LD and HD refer to low-density C-S-H and high-density C-S-H, respectively.
[b] Assuming Poisson's ratio of 0.27 [35].
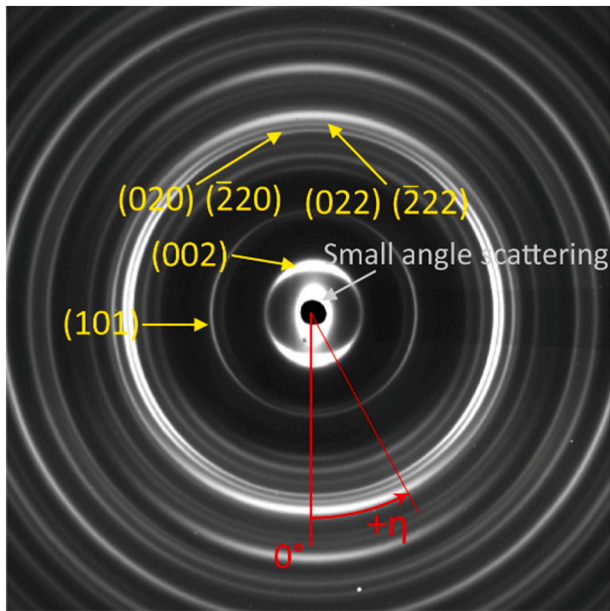[c] Assuming Poisson's ratio of 0.26 [35].
[d] Indentation depth. The scale of volume is a few times of the indentation depth.

Fig. 3. Raw 2D diffraction image of the dry non-holding 200 MPa C-A-S-H compact; the zero-azimuth and the positive direction are indicated in red; selected diffraction rings are indicated in yellow. (For interpretation of the references to color in this figure legend, the reader is referred to the web version of this article.)

(Fig. 3) was sliced into 72 segments, each spanning an azimuthal angle of 5°. 72 diffraction patterns were obtained by integration over each 5°, as inputs for the subsequent texture analysis.

Due to the symmetry of loading with the compression die, the texture model of a standard fiber function is utilized to describe the orientation distribution function (ODF) developed in the compacts of nanocrystalline C-A-S-H, portlandite, or ettringite. Note that the term fiber here does not refer to the morphology of a nano grain or a single crystal but denote that the crystal/granular orientation has a preferred axis. The sample position was set with ω = 90° so that the center of the pole figure is brought to the normal of the compact – i.e., parallel to the compression direction (Fig. 2).

The orientation of the fiber component is defined with reference to 1) the sample normal and 2) the orientation axis in the unit cell [56–57]. The definition of the fiber component in MAUD with respect to the sample normal is given by the parameters PhiY (the azimuthal angle) and ThetaY (the polar angle). Regarding the geometry of the experiment, ThetaY corresponds to the small difference between the compression direction to the absolute vertical direction (the x-axis), which is expected to vary slightly around 0° due to misalignments in compact placement; the value of PhiY is free for refinement. The definition of the fiber component with respect to the unit cell is through ThetaH, the azimuthal angle around the c-axis, and PhiH, the polar angle starting from the c-axis. In the present study, both ThetaH and PhiH are fixed to 0, due to the observed alignment of the c-axis of the C-A-S-H to the compression direction.

A pure Gaussian fiber component was used to describe the ODFs in this study since previous texture analysis on similar phases using standard fiber function reported negligible Lorentzian fiber component or random texture component [35]. The width of the Gaussian fiber component was refined through the parameter FWHM (full width at half maximum).

The d^{-1} ranges of interest were selected for texture analysis using Rietveld refinement: for C-A-S-H samples, (002) plane and the rest labeled planes (up to d^{-1} of ~0.38 Å^{-1}) were analyzed separately; Wider d^{-1} range were considered for the refinement of portlandite (up to ~0.71 Å^{-1}) and ettringite (up to ~0.63 Å^{-1}) due to their higher

crystallinity. Background functions, diffraction intensity, unit cell parameters, and standard fiber function parameters were refined while instrument parameters were calibrated with the XRD measurement of CeO$_2$ and fixed throughout the analysis. Pole figures of selected planes were generated for each sample based on the refined texture where multiples of random distribution (m.r.d.) is the parameter to characterize the strength of the developed preferred orientation of certain planes.

3. Results

3.1. C-A-S-H

The raw 2D XRD diffraction image of each sample was integrated over 72 segments each of 5° azimuthal angle. The diffraction intensity as a function of the azimuthal angle was obtained (Fig. 4a), and the selected patterns were presented with featured diffraction peaks labeled (Fig. 4b).

As observed intuitively from the pattern stacks, strong texture was quantified for the compressed C-A-S-H. The (002) lattice plane showed especially intense preferred orientation, implicating the anisotropy of C-A-S-H nanocrystallites. This deviatoric stress-induced preferred
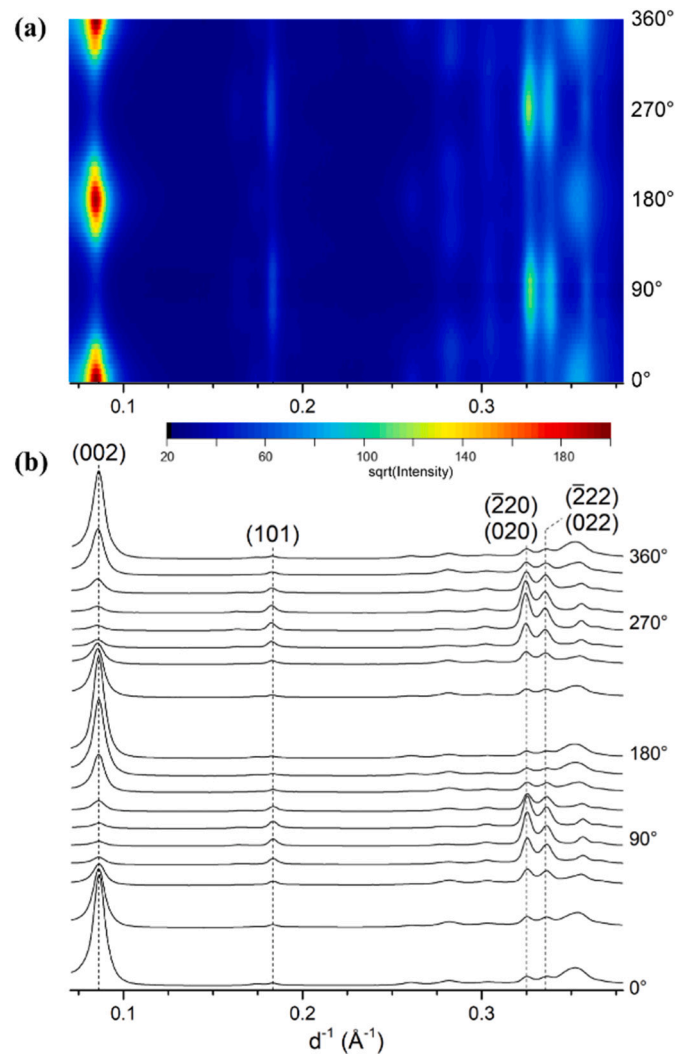
Fig. 4. (a) Stack of diffraction intensity as a function of azimuthal angles and (b) measured diffraction patterns at selected azimuthal angles, aligned with (a), corresponding to the raw diffraction image in Fig. 3 (the dry non-holding 200 MPa C-A-S-H compact).

orientation is often found in geological materials, including layered silicate phases, e.g., clay minerals (kaolinite and illite [58–59]). The crystal preferred orientation of C-A-S-H can be attributed to the rotation and re-orientation of C-A-S-H nanocrystallites, not necessarily meaning an agreement or disagreement with the dissolution-recrystallization creep theory [40] or the CM-II colloid model [60].

The reference loose powder sample of C-A-S-H did not show the development of any preferred orientation comparable to those observed in the compacts (Fig. 5). The refined m.r.d. of the reference samples were essentially ~1, confirming the truly random orientation under undisturbed conditions, i.e., prior to the compression.

Different degrees of texture were quantified in all C-A-S-H compact samples. The small values of the refined ThetaY confirm the slight misalignment between the compact's central axis and the absolute vertical. The (002) basal diffraction peak developed the strongest preferred orientation in each compact compared to other (hkl) planes; and in all cases, [002] direction primarily aligned with the compression direction– referring to the anisotropic morphology of C-A-S-H (crystal size refined with the reference sample, see Table S1 in Supporting Information), the larger dimensions (a,b-plane) of the disk-like nanocrystallites became perpendicular to the compression direction, and the nanocrystallites subsequently stacked with their short dimension (the c-axis) parallel to the compression.

Holding of the 200 MPa load for 300 s intensified the texture, as seen from narrow FWHM and great max. m.r.d. (Table 2 and Fig. 6), revealing the time-dependent nature of the stress-induced re-orientation of C-A-S-H nanocrystallites. A schematic for the meaning of pole figures is illustrated in Fig. 7. This time-dependence of texture with constant stress has been evidenced in geological studies, and has been correlated to the creep of materials [62]. Increasing the maximum load resulted in stronger texture as well. This fact can be attributed to that greater energy provided to the system so that the friction between nanocrystallites could be more frequently overcome and their re-orientation is facilitated. Regardless of relative humidity, by comparing 200 MPa-no holding to either 200 MPa-holding or 500 MPa-no holding, the effect of load holding was more significant than the effect of increasing the instantaneous maximum load, reaffirming the time-dependent nature of

the development of preferred orientation of C-A-S-H. Comparing each pair of C-A-S-H (RH100%) and C-A-S-H (dry) through same loading processes, the RH100% sample consistently developed greater preferred orientation of (002), as seen from narrower FWHM and greater m.r.d. The RH100% compact after a hold at 200 MPa exhibited the highest max. m.r.d., the lowest min. m.r.d., and the smallest FWHM. This fact indicates that water may serve as a lubricant in the matrix, promoting the re-orientation of C-A-S-H nanocrystallites. Water-induced preferred orientation has been found in geological samples, e.g., olivine [63–64].

The texture quantification using a higher range of d^{-1}, not overlapping with the range for analyzing (002), was conducted to characterize the development of preferred orientation of a- and b-axis of C-A-S-H. Calculated pole figures for (200) and (020) demonstrate that the a- and b-axis of C-A-S-H nanocrystallites were preferentially orientated radially and perpendicularly to the compression direction (Fig. 8), agreeing with the expected positioning of the a,b-plane (i.e., parallel to (002)) in consideration of the axially symmetric geometry of the loading process and the calculated [002] preferred orientation to the compression direction. Note that, all [h00] and [0k0] directions (normal to (h00) and (0k0) planes, respectively) are parallel a- and b-axis, respectively, of the unit cell; thus, the display of (200) and (020) pole figures suffices to illustrate the preferred orientation in terms of the a- and b-axis.

The influence of moisture content, maximum loading, and holding of the load on the preferred orientation of (020) and (200) agrees with that obtained from analyzing the (002) basal diffraction: the RH100% compacts constantly developed stronger texture than their dry counterparts; both increasing loads and holding loads resulted in stronger texture while the effect of holding was more noticeable, consistent with the trends learned from analyzing (002). The FWHMs of the fiber component refined from the two d^{-1} ranges generally agree well with each other. Whereas, the m.r.d. of (200) and (020) were much lower than that of (002), in all samples, due to the radially distributed (200)/(020) orientations toward the perimeter of the pole figure as opposed to the (200) alignments concentrated at the pole.

The unit cell parameters were refined at the meantime of texture quantification (Table 3). The range in basal spacing comes from the slight variation in (002) peak position over different azimuthal angles due to the strain distribution in this deviatoric stress setup. This wavy azimuthal strain distribution is commonly observed and more noticeable in geological samples under higher deviatoric stress [65]. The a- and b-axis residual strains in the compacts, compared to the ambient-condition references, were within ±0.3%. The basal spacing of RH100% C-A-S-H compacts were systematically larger than that of their dry counterpart by 0.8% just because the initial basal spacing of RH100% reference was slightly larger than the dry reference due to the dehydration of the dry reference. Holding of the load does not affect the c-axis residual strain while 0.3% greater compressive residual strain remained in the compacts having endured 500 MPa, regardless of the moisture condition. This observation could be explained by the fact that the nanocrystallites were more compacted after loading at 500 MPa, and the tighter interlocking between nanocrystallites prevented a full recovery of residual strains.

3.2. Portlandite and ettringite

The same compression procedures were applied to portlandite as RH100% or dry C-A-S-H while only one ettringite compact was processed with non-holding 200 MPa maximum loading. In all situations, moderate preferred orientations were developed in the compacted portlandite and ettringite compacts (Table 4). See examples in Fig. S1 in Supporting Information. For portlandite, both holding the compressive load and increasing the load led to stronger texture development. Specifically, compared to the non-holding 200 MPa compact of portlandite, increasing the compressive load (500 MPa, no holding) had greater contribution to texture formation than holding the loading (200 MPa, holding) did, in contrast to the case of C-A-S-H, suggesting that time-
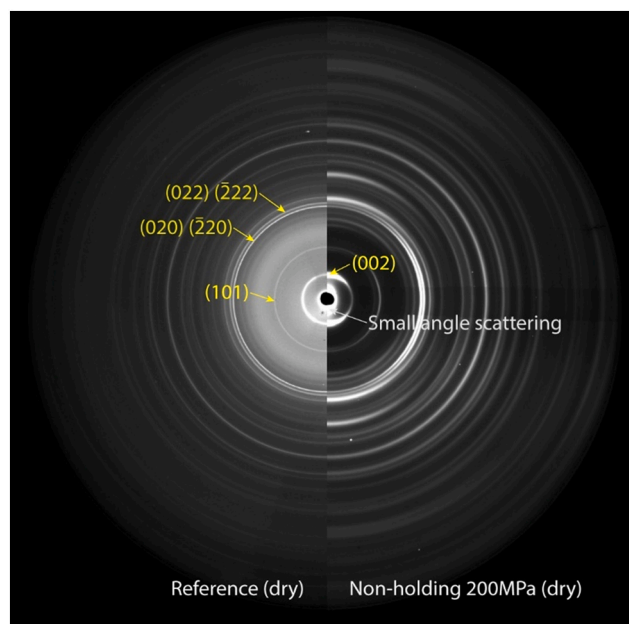

Fig. 5. Raw 2D diffraction image of the dry C-A-S-H reference (left) and the dry non-holding 200 MPa compact (right). A shadow from the absorption of glass capillary used for the reference measurement (left) was found, but it does not affect the other azimuthal angles.

Table 2

Texture information of C-A-S-H lattice planes (002), (200), and (020). Planes (200) and (020) have equal m.r.d., because both planes are perpendicular to the direction of the standard fiber component with respect to the unit cell.

	Loading condition	(002) plane			(200) and (020) planes	
		FWHM	m.r.d. (min.–max.)	ThetaY	FWHM	m.r.d. (min.–max.)
C-A-S-H (RH100%) Rwp[a] = 11–12%	200 MPa, holding	24.4	0.02–15.4	−9.0	49.7	0.20–1.94
	200 MPa, no holding	49.9	0.18–7.6	−3.5	49.8	0.24–1.53
	500 MPa, no holding	47.7	0.15–8.3	−4.2	46.3	0.36–1.68
C-A-S-H (dry) Rwp[a] = 11–12%	200 MPa, holding	50.3	0.25–7.5	−6.9	46.9	0.52–1.75
	200 MPa, no holding	56.4	0.26–6.1	−4.6	56.7	0.42–1.48
	500 MPa, no holding	55.8	0.26–6.2	−7.8	52.2	0.39–1.53

[a] The value of Rwp in texture analysis using 72 diffraction patterns is often much higher than that in conventional powder diffraction (using a single pattern) [61]; and an Rwp value of 15% is very good for texture analysis of highly crystalline phases [61]. Therefore, the Rwp values of 11–12% obtained from the textured nanocrystalline C-A-S-H indicate that the refinements were done satisfactorily in the present study.
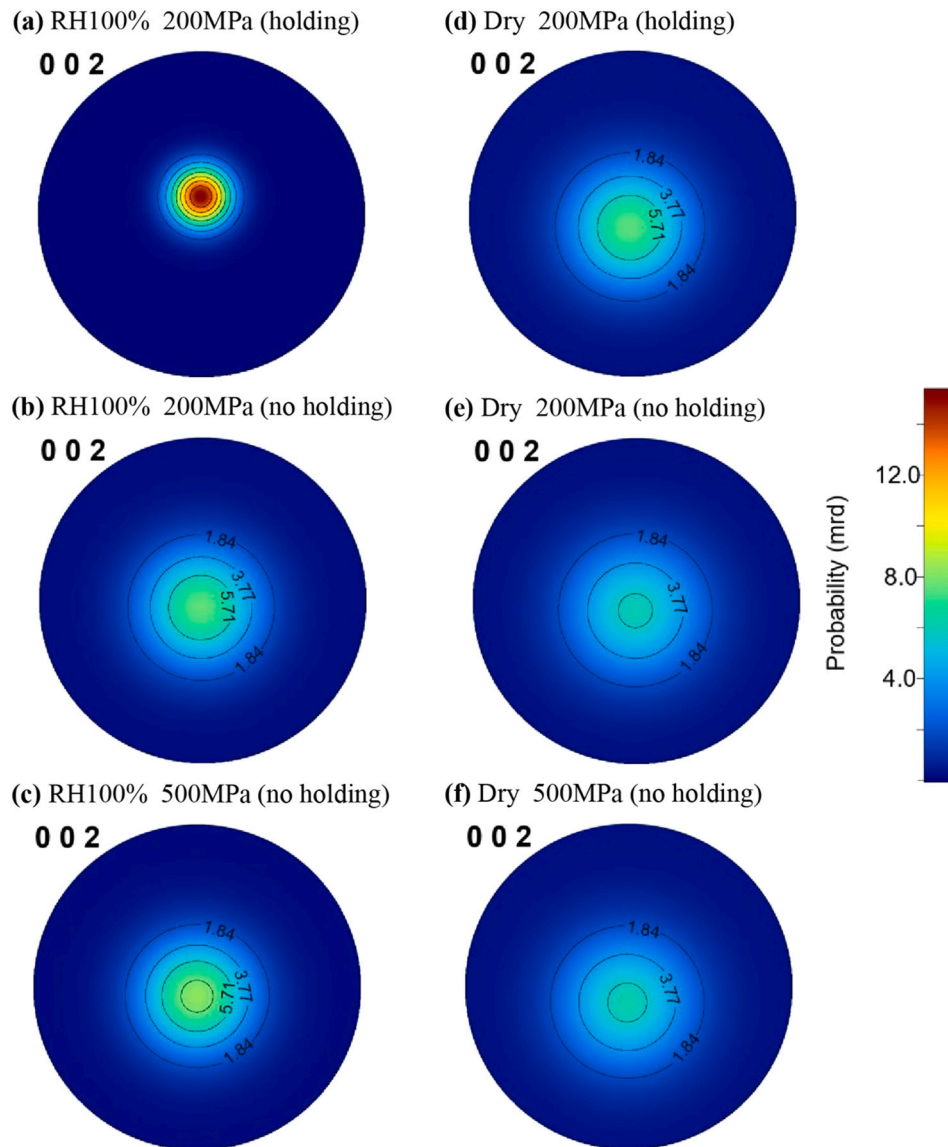
Fig. 6. Pole figures of C-A-S-H plane (002) under different conditions. Compression direction is approximately in center of pole figures. Numbers in the pole figures are probability values. A schematic for the meaning of pole figures is illustrated in Fig. 7.

dependency is less relevant to the re-orientation of portlandite crystals than it is to that of C-A-S-H. Ettringite presented similarly modest texture feature as portlandite, as evidenced from comparable m.r.d. of their non-holding 200 MPa compacts. At the same loading condition, both portlandite and ettringite exhibited greater FWHM and significantly narrower m.r.d. range relative to C-A-S-H, indicating their considerably lower susceptibility to preferential re-orientation due to compressive loading.

Pole figures calculated from the three portlandite compacts were similar in their pattern despite different m.r.d. ranges. The portlandite
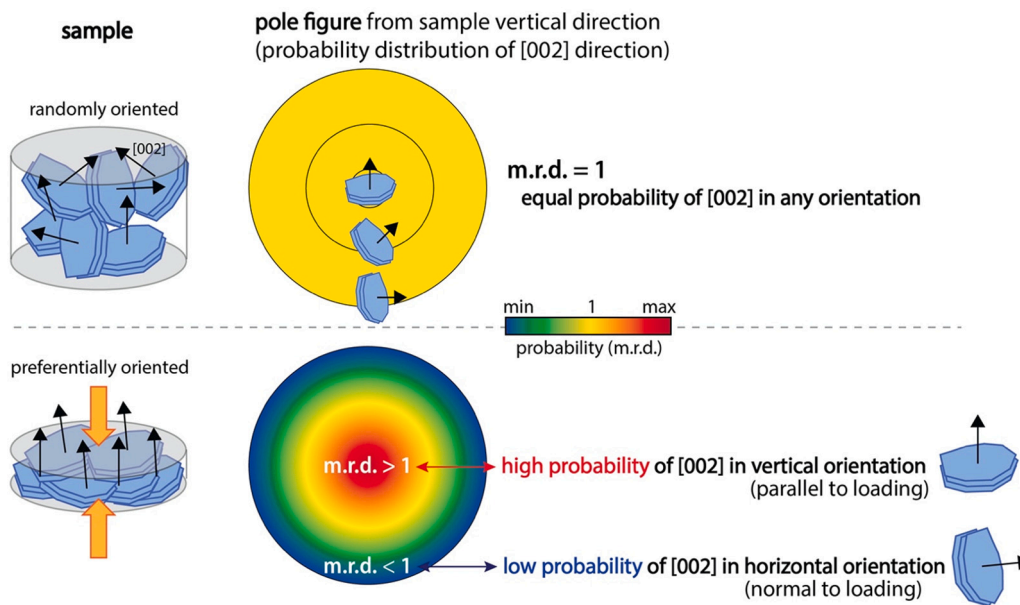
Fig. 7. A schematic for the meaning of pole figures. C-A-S-H is shown as an example.
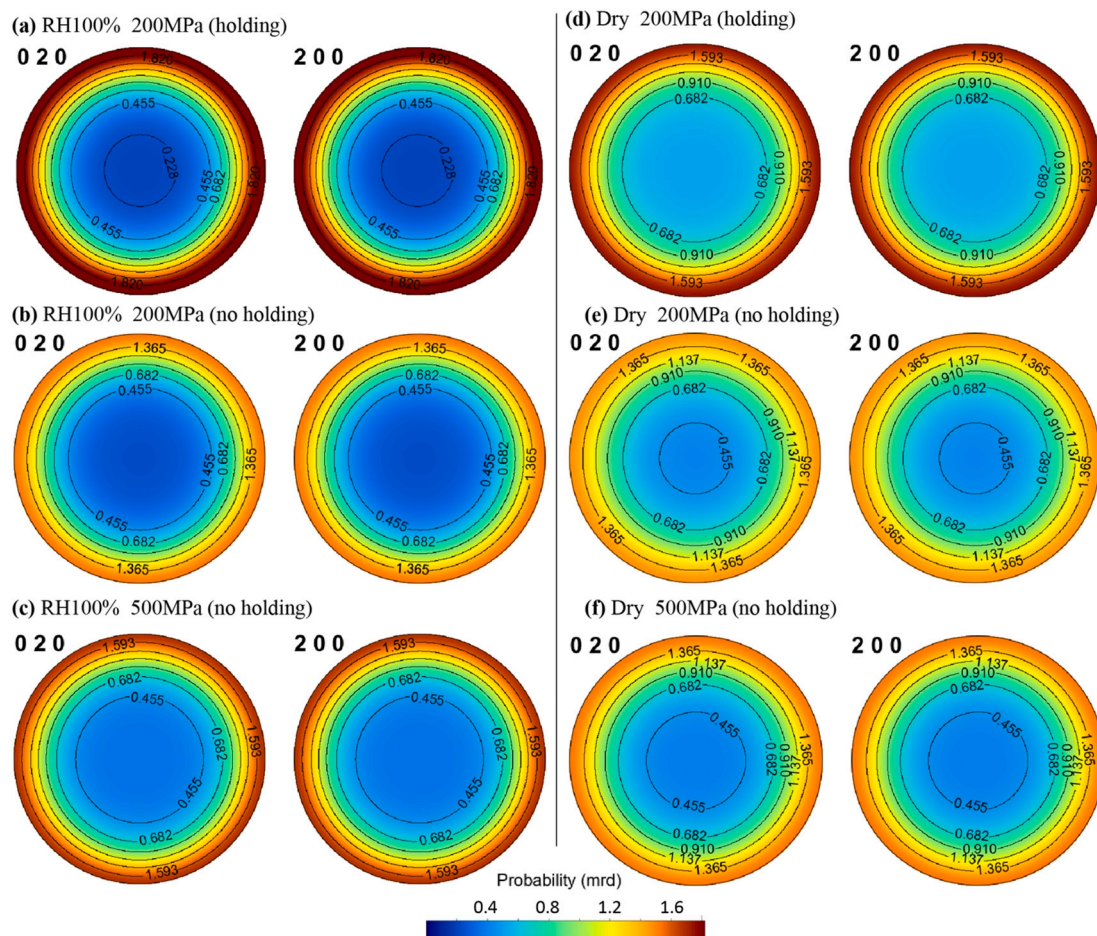
Fig. 8. Pole figures of C-A-S-H planes, (020) and (200) under different conditions. Compression direction is approximately in center of pole figures. Numbers in the pole figures are probability values.

[001] direction tended to incline toward the pole in spite of the limited extent. In relation to the platy shape of a typical portlandite crystal (the c-axis being the short dimension), the platy crystals were subject to aligning the c-axis to the compression direction (Fig. 9a), in analogue to the case of disk-like C-A-S-H nanocrystallites, albeit the considerably weaker preferred orientation of portlandite.

Table 3

Unit cell parameters of C-A-S-H samples, with γ fixed at 123.18°. The errors for lattice parameters a and b are 0.001 Å and the error for c is 0.01 Å.

		a (Å)	b (Å)	c (Å)	Basal spacing (Å)
RH100%	No loading, reference	6.713	7.387	23.34	11.67
	200 MPa, holding	6.710	7.376	23.32–23.44	11.66–11.72
	200 MPa, no holding	6.711	7.373	23.28–23.42	11.64–11.71
	500 MPa, no holding	6.679	7.394	23.24–23.38	11.62–11.69
Dry	No loading, reference	6.706	7.381	23.18	11.59
	200 MPa, holding	6.693	7.383	23.12–23.26	11.56–11.63
	200 MPa, no holding	6.697	7.401	23.12–23.24	11.56–11.62
	500 MPa, no holding	6.707	7.376	23.08–23.18	11.54–11.59

Upon compression, the hexagonal needle-like ettringite crystals (growing along the c-axis) tended to have the longest dimension perpendicular to the maximum loading: in the pole figure centered with the compression direction (Fig. 9b), [002] direction (i.e., longitudinal to the ettringite needles) were more distributed around the perimeter while [100] direction (i.e., transverse) were concentrated toward the pole. Yet, the texture of ettringite through the same loading process was not as strong as that in C-A-S-H – the range of m.r.d. was ~0.6 for ettringite compared to >6 for C-A-S-H. In all samples, the compression process did not result in noticeable residual strain of the unit cells of portlandite or ettringite (Table 4).

4. Discussion

The driving force of the re-orientation of C-A-S-H crystallites is the vertical deviatoric stress from the compression load. The re-orientation of C-A-S-H crystallites in the present study was likely facilitated by the inter-grain motion (e.g., glide and rotation). Higher deviatoric stresses result in higher packing density of the pellets (i.e., lower porosity) [20–21]. The lower porosity, i.e., shorter inter-grain distance, fails to act as a barrier for the inter-grain motion because the deviatoric stress dominate the inter-grain motion of crystallites. If the pore structure of the dry pellet, e.g., capillary pore, plays a dominate role in the preferred orientation of crystallites, the higher stress induced refined pores would limit the development of crystallite orientation. The probed sample volume in this experiment is ~30 μm³, which already includes capillary pores. Thus, our observation does not support the capillary's influence on crystallite orientation of dry pellets at any scale. This inter-grain motion is suggested to be aided by gel-pore water. The evaporable water content in C-A-S-H at RH > 75% was significantly higher than that in freeze-dried C-A-S-H (using the same batch samples, evidenced by

thermogravimetric analysis in [21]). This evaporable water was ascribed mainly to gel-pore water instead of interlayer water, indicating an important difference in inter-grain environment between C-A-S-H with high and low moisture contents. Thus, in RH100% samples (Fig. 10a), gel-water is suggested to act as lubricants, reducing the resistance to inter-grain motion, resulting in stronger preferred orientation of the nanocrystallites compared to dry C-A-S-Hs with negligible gel-water content (Fig. 10b). This water lubrication agrees with [66] where a decay of sliding free energy barrier as granular distance increases was found and [36] where higher water content of C-S-H results in more creep.

Other types of motion/transformation of C-(A-)S-H are less likely to dominantly promote the texture formation in C-A-S-H, compared to the lubrication effect of gel-pore water. While interlayer sliding has been observed in C-S-H under compressive pressure [67], it is unlikely to be accounted for the texture formation of C-A-S-H in the present study because the C-A-S-H was cross-linked (strong Si—O—Si/Al bonds) with limited interlayer water content, both factors inhibiting interlayer sliding. Moreover, a transformation through the dissolution-precipitation mechanism, observed in olivine [64] – where high pressure and high temperature induced increase in silicate solubility to enable texture formation through recrystallization – is unlikely responsible for the herein observed C-A-S-H textures because this mechanism requires the stressing process be considerably extended to the scale of hours, the magnitude of the applied pressure be raised to the scale of GPa, and the temperature be significantly elevated (>1000 °C). Considering the low stress, low temperature, short span of time scale, low gel-pore water content, and low solubility of Si in the present study but a strong preferred orientation, a proposed dissolution-precipitation mechanism [68] for the creep of C-S-H seems questionable. Therefore, the lubrication effect owing to gel-water is suggested to be a main driving force behind the texture development in cross-linked C-A-S-H compacts.

The time-dependent development of the preferred orientation of C-A-S-H in this study can shed light on the fundamental time-dependent phenomenon in cement-based materials. The development of creep strain over time could originate from the gradual gaining of preferred-orientation of C-A-S-H nanocrystallites (Fig. 11a). This stress-induced re-orientation of nanocrystallites results in a more compacted micro-structure (higher packing density) and agrees with the nanogranular mechanism of cement creep [38]. Increased creep strain at elevated stress levels [69] and/or higher moisture content [70] can be correlated to the herein observed more intense texture development of C-(A-)S-H under these conditions. This origin of creep of cement-based materials could supplement the previously proposed creep mechanisms – e.g., the interlayer sliding of C-S-H [39,71] and the crystallization and formation of new interlayer spaces [72] – especially in cases of creep where the interlayer sliding is inhibited by interlayer cross-linking or where a short-term creep is incompatible with the time-consuming crystallization process or interlayer bond breakage and reformation.

In addition, the present experimental findings regarding the

Table 4

Texture information and unit cell parameters of portlandite and ettringite compacts after removal of the loading. Listed m.r.d. are for portlandite (001) and ettringite (002).

	Loading condition	(00l) plane			Unit cell parameters (Å)	
		FWHM	m.r.d. (min.–max.)	ThetaY	a	c
Portlandite						
	Reference, no pressure	–	1	–	3.5898	4.9093
Rwp = 7–9%	200 MPa, holding	131.9	0.80–1.42	−7.5	3.5882	4.9098
	200 MPa, no holding	154.5	0.88–1.24	3.5	3.5898	4.9113
	500 MPa, no holding	121.5	0.74–1.51	4.2	3.5890	4.9121
Ettringite						
	Reference, no pressure	–	1	–	11.2344	21.4699
Rwp = 17%	200 MPa, no holding	60.6	0.61–1.21	−3.1	11.2337	21.4737
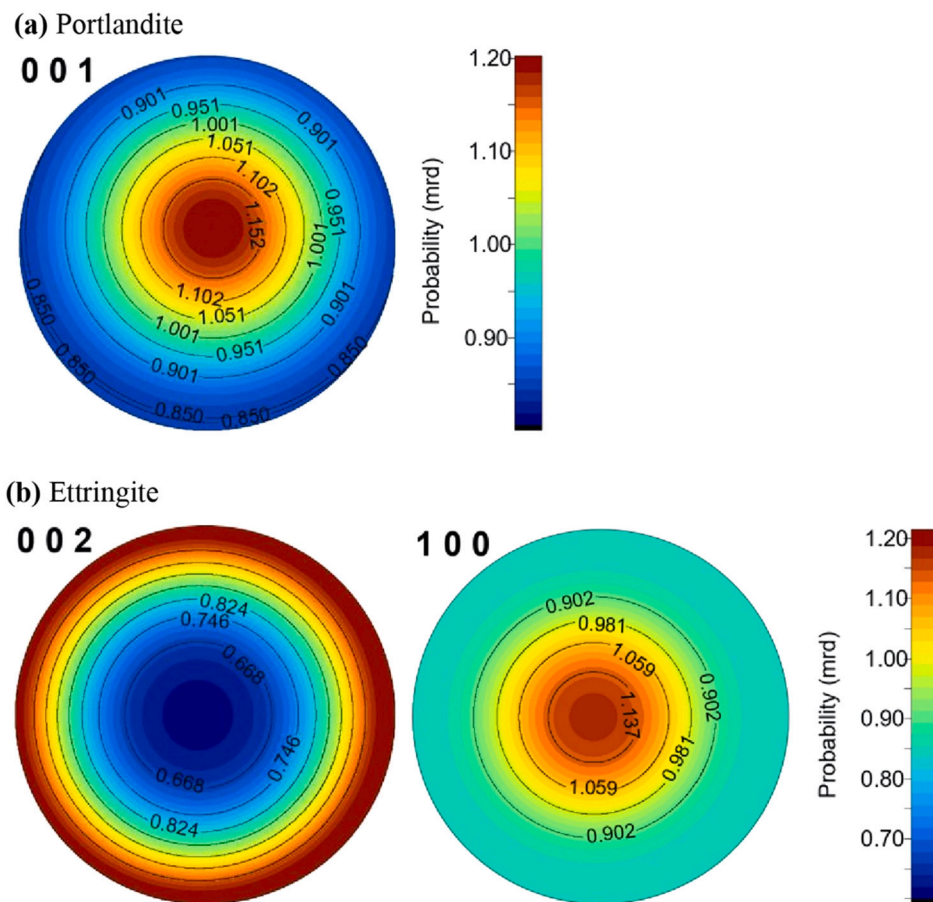
Fig. 9. Pole figures of (a) portlandite plane (001) calculated from the non-holding 200 MPa compact and (b) ettringite planes (002) and (100) calculated from the non-holding 200 MPa compacts. Compression direction is approximately along the center of the pole figure. Numbers in the pole figures are probability values.
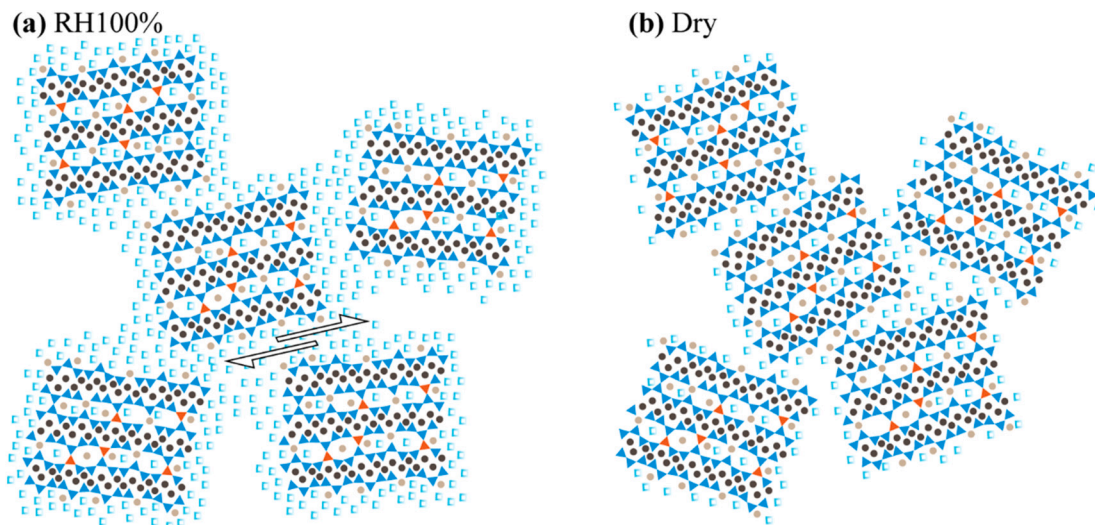
Fig. 10. Schematic representation of the effect of water on the development of preferred orientation of C-A-S-H nanocrystallites. (a) C-A-S-H compact at RH 100%; (b) freeze-dried C-A-S-H compact. Blue and orange triangles denote SiO_4 and AlO_4, respectively; dark and light brown circles represent intralayer and interlayer Ca, respectively; light blue squares represent water molecules; arrows demonstrate a possibility of water-facilitated gliding between C-A-S-H nanocrystallites. (For interpretation of the references to color in this figure legend, the reader is referred to the web version of this article.)

behavior of portlandite crystals are also consistent with creep test results on cement pastes. Higher portlandite content was related to smaller the creep coefficient in [73]. This fact could be interpreted that portlandite has limited degree of compression-induced preferential re-orientation

and thus minimal contribution to creep of cement paste (Fig. 11b). It is expected that the role of ettringite to the creep of cement paste is similarly insignificant as to that of portlandite (Fig. 11c).

The developed texture patterns could be correlated to the anisotropic

(a) C-(A-)S-H

(b) Portlandite
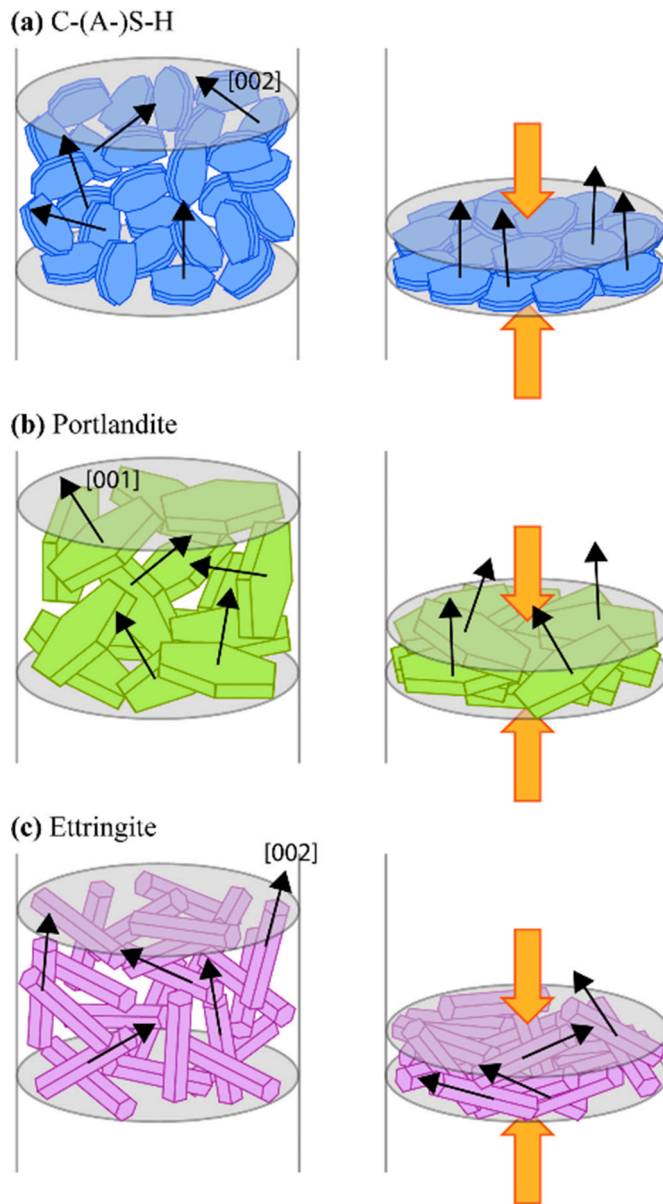
(c) Ettringite

Fig. 11. Schematic representation of the development of preferred orientation of (a) C-(A-)S-H, (b) portlandite, and (c) ettringite crystals after compaction. Orange arrows represent compressive load, and black arrows represent the induced [001] or [002] direction. C-(A-)S-H is known to have long-range ordering along the a- and b-axes only. (For interpretation of the references to color in this figure legend, the reader is referred to the web version of this article.)

mechanical properties of the crystals. The a- and b-axis incompressibility of C-(A-)S-H unit cells ranges within ~250–350 GPa, and the c-axis incompressibility ranges within ~70–230 GPa [23–24,74–75]. C_{11}/C_{33} of portlandite was reported to be 3.03 [3], and that of ettringite was reported to be 0.64 [2]. Note that for both C-(A-)S-H and portlandite, the c-axis is the softest unit-cell axis and their c-axis both tend to align with the compression while for ettringite, the c-axis is the stiffest and its c-axis tends to be perpendicular to the compression. Thus, it is suggested that for these primary phases in hydrated cement paste, the crystals develop preferred orientation such that the softer dimension becomes more aligned with the compressive stress.

The observation of strong texture formation in C-A-S-H after loading to 200 MPa and then unloading in the present study suggests that extra precaution or qualification is required for a valid interpretation of nano-

and even micro-indentation-characterized mechanical properties of C-(A-)S-H or cement-based materials. In the case of an indentation experiment on hardened paste samples (or alkali-activated blast-furnace slag paste), the originally randomly oriented C-(A-)S-H nanocrystallites are subject to preferentially re-orientation near the indenter (Fig. 12a) in response to high stress levels [13,38,76], typically one order of magnitude greater than in the present compact preparation process or even higher due to local stress concentration near the indenter [77]. In the case of an indentation experiment on a prepared C-(A-)S-H compact (Fig. 12b), there already exists preferred orientation of C-A-S-H nanocrystallites in the compact, and the indentation process is expected to alter the preferred orientation pattern local to the indenter as well as a few μm^3 of probed interactive volume.

It is conventionally assumed that indentation experiments, through large number of sampling, could yield information about the bulk properties of materials. However, our findings suggest that the indentation experiment tends to over-represent the mechanical properties along the c-axis, which could result in underestimation of the elastic modulus and hardness of C-(A-)S-H for the c-axis being the softest unit cell axis. Indeed, the nano-indentation modulus of C-S-H was measured to be lower than that of cross-linked C-A-S-H in [21]: this result is likely a reflection of the lower c-axis stiffness of C-S-H compared to cross-linked C-A-S-H [23] rather than a faithful indication of the difference in their bulk mechanical properties. For this reason, in order for an indentation experiment to explore the bulk properties of a C-(A-)S-H-based material under service conditions, lowering the applied pressure is an approach to avoid overrepresentation of the c-axis. For example, a creep test using micro-indentation performed at ~2 MPa ([73]) would prevent rapid preferential alignment of the c-axis so as to preclude nonpractical creep coefficient measurements.

A recent microindentation study [80] described two creep mechanisms of cement pastes: the reversible short-term creep mechanism and long-term logarithmic creep mechanism. Further investigations are needed to understand which creep mechanism is dominated by the preferred orientation of C-(A-)S-H nanocrystallites. Given that the preferred orientation is irreversible in our study, it is more likely that the preferred orientation is the origin of long-term logarithmic creep of cement-based materials.

As cement-based materials are hierarchically porous, determining the multiscale mechanical properties is crucial. Characterization techniques at different scales can be harnessed to improve the understanding of the multiscale mechanical properties of cement-based materials. HP-XRD is a powerful tool to determine the mechanical properties of nanocrystalline and crystalline materials at the unit cell scale (i.e., the pore-free level). Recent advances in high-pressure techniques allow to determine the mechanical properties of phase-pure amorphous materials (e.g., alkali-silica reaction gel, ASR gel) at the pore-free level [81] with HP-XRD and to determine the mechanical response of Ca—O and Si—O pairs with high-pressure X-ray Raman and optical Raman [67,82]. However, currently high-pressure techniques may not be capable of determining the mechanical properties of the complex poorly crystalline C-(A-)S-H in cement pastes. Compared to nanocrystalline C-(A-)S-H, poorly crystalline C-(A-)S-H that typically formed in cement pastes has a similar layered structure with poorer layer-stacking ordering and more defects [83]. The formation of nanocrystalline C-(A-)S-H requires a high volume of (alumino)silica(te) in Portland cement-based materials or lime-based systems. For example, nanocrystalline C-(A-)S-H has been found in high-volume fly ash cement pastes [84], ancient Roman concrete [85], and alkali-activated blast-furnace slag. Thus, the learned knowledge of C-A-S-H crystallite preferred orientation from XRD can be partially applied to realistic cement-based systems. Although nanoindentation has the aforementioned influence regarding the preferred orientation of layer-structured phases, nanoindentation has no such limitation on the crystallinity of phases in cement pastes compared to HP-XRD. A recent study has shown that coupling nanoindentation with chemical mapping can probe the mechanical properties of C-(A-)S-H at a
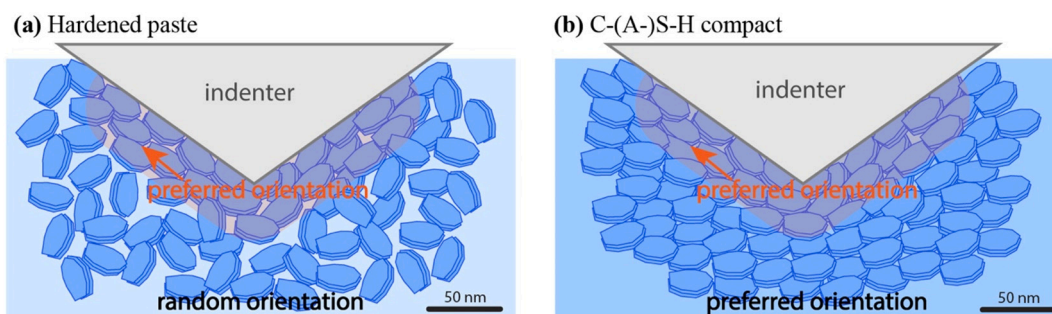
Fig. 12. Schematic representation of the development of preferred orientation of C-(A-)S-H nanocrystallites during nanoindentation experiments using (a) hardened paste (e.g., high volume fly ash cement or alkali-activated blast-furnace slag) and (b) C-(A-)S-H compact. The development of texture of samples in microindentation experiments is similar to that nanoindentation. Note that, the schematic is only for the illustration of the nano- and micro-structure of specimens around the indenter. The overall probed interactive volume of an indenter can be a few times deeper than the maximum indentation depth [78–79]. This significantly large probed interactive volume is not fully illustrated here.

phase-pure but porous level in heterogeneous systems, such as high-volume natural pozzolan concrete [86]. Nanoindentation can probe the mechanical properties of cement phases at submicron or microns level by reflecting pore structures' effect. Thus, nanoindentation may reflect the influences of water-to-binder ratios, degree of hydration, and curing temperature [13] on the micromechanical properties of porous C-(A-)S-Hs. Similarly, microindentation can also probe the mechanical properties of porous cement pastes but with much larger interactive volume, e.g., hundreds of μm^3. Thus, microindentation either reflects the mechanical properties of porous mixed phases (e.g., a mixture of C-S-H and portlandite) or porous synthetic pure phases (e.g., C-S-H) [22]. Microindentation would be more representative if the research interest is regarding the bulk mechanical properties of cement-based materials, particularly related to microstructure.

Further investigations on the creep behavior of C-A-S-H compacts are needed. A systematical experimental study of synthetic C-(A-)S-Hs with varying compositions (e.g., Ca/(Al + Si) and Al/(Al + Si) ratios) will be informative. A comparison of the nanogranular orientation between synthetic nanocrystalline C-(A-)S-H compacts and poorly crystalline C-(A-)S-H in cement-based materials will be interesting. Small-angle scattering with a two-dimensional detector may be an efficient tool to probe the nanogranular orientation and inter-grain motion of poorly crystalline C-(A-)S-Hs in cement pastes. This technique can be applied to validate the nanogranular orientation of cement pastes under sustained compressive stress.

5. Conclusions

The preferred orientation of cross-linked C-A-S-H, portlandite, and ettringite crystals were studied with synchrotron-radiation-based XRD, using compacts after removal of compressive stress of (holding for 300 s or non-holding) 200 or 500 MPa. The effects of water content on the preferred orientation of cross-linked C-A-S-H were investigated. Based on the aforementioned results, the following conclusions can be draw:

1. Strong texture (i.e., crystals preferred orientation) formed in all C-A-S-H compacts. The c-axis of C-A-S-H nanocrystallites became highly aligned to the compression direction while the a- and b-axis lay perpendicular to the compression direction. Stronger preferred orientations were developed for compacts at high relative humidity, having endured a holding load for 300 s, and/or having experienced a higher stress level.
2. Higher water content of cross-linked C-A-S-H results in stronger preferred orientation. The texture formation in the cross-linked C-A-S-H was primarily facilitated by the gel-pore water rather than interlayer sliding or recrystallization.
3. The water-facilitated and time-dependent natures of the texture development of cross-linked C-A-S-H provide new insights on the

mechanism of creep in cement-based materials. The pressure-induced gradual preferential re-orientation of C-A-S-H nanocrystallites could be accounted for the creep development while portlandite and ettringite with limited degree of texture formation would have limited contribution to creep of cement-based materials.
4. Portlandite and ettringite compacts showed moderate preferred orientations compared to cross-linked C-A-S-H. The c-axis of portlandite (the central axis of a plate-like portlandite crystal) tended to align more with the compression direction while the c-axis of ettringite (the longitudinal direction of a needle-like ettringite crystal) tends to lie more perpendicular to the compression direction.
5. The preferred orientation of the typically softer c-axis of cross-linked C-A-S-H to the compression direction suggests that nano/micro-indentation experiment at elevated stresses could be biased toward the mechanical properties of c-axis and underestimate the modulus of the bulk material.

XRD with a two-dimensional detector is a powerful tool to quantify the stress-induced preferred orientation of crystallites. The developed technique with a probed interactive volume of ~30 μm^3 can truly reflect the unit-cell structural change and the nanogranular behavior of nanocrystallites. The method can be used to study the effects of water content, compositions, stress level, and time dependence on the nanogranular motion of (nano)crystalline materials. The technique is also promising to represent the nanogranular orientation of nanocrystalline C-(A-)S-Hs in cementitious systems, e.g., high volume fly ash cement, roman concrete, and alkali-activated blast-furnace slag. A deeper understanding of the cementitious system with nanocrystalline C-(A-)S-Hs will provide new insight into understanding the creep mechanism of cementitious materials and designing cementitious materials with low creep compliance.

CRediT authorship contribution statement

Jiaqi Li: Conceptualization, Methodology, Formal analysis, Investigation, Validation, Visualization, Writing - Original Draft.
Wenxin Zhang: Formal analysis, Visualization, Writing - Review & Editing.
Paulo Monteiro: Conceptualization, Writing - Review & Editing, Supervision, Funding acquisition.

Declaration of competing interest

The authors declare that they have no known competing financial interests or personal relationships that could have appeared to influence the work reported in this paper.

Appendix A. Supplementary data

Supplementary data to this article can be found online at https://doi.org/10.1016/j.cemconres.2021.106371.

References

[1] B. Pichler, C. Hellmich, Upscaling quasi-brittle strength of cement paste and mortar: a multi-scale engineering mechanics model, Cem. Concr. Res. 41 (2011) 467–476.

[2] S. Speziale, F.M. Jiang, Z. Mao, P.J.M. Monteiro, H.R. Wenk, T.S. Duffy, F. R. Schilling, Single-crystal elastic constants of natural ettringite, Cem. Concr. Res. 38 (2008) 885–889.

[3] S. Speziale, H.J. Reichmann, F.R. Schilling, H.R. Wenk, P.J.M. Monteiro, Determination of the elastic constants of portlandite by Brillouin spectroscopy, Cem. Concr. Res. 38 (2008) 1148–1153.

[4] J.S. Dolado, M. Griebel, J. Hamaekers, A molecular dynamic study of cementitious calcium silicate hydrate (C-S-H) gels, J. Am. Ceram. Soc. 90 (2007) 3938–3942.

[5] H. Manzano, J.S. Dolado, A. Guerrero, A. Ayuela, Mechanical properties of crystalline calcium-silicate-hydrates: comparison with cementitious C-S-H gels, Phys. Status Solidi A 204 (2007) 1775–1780.

[6] K. Garbev, G. Beuchle, M. Bornefeld, L. Black, P. Stemmermann, Cell dimensions and composition of nanocrystalline calcium silicate hydrate solid solutions. Part 1: synchrotron-based X-ray diffraction, J. Am. Ceram. Soc. 91 (2008) 3005–3014.

[7] E. L'Hôpital, B. Lothenbach, D. Kulik, K. Scrivener, Influence of calcium to silica ratio on aluminium uptake in calcium silicate hydrate, Cem. Concr. Res. 85 (2016) 111–121.

[8] R.J. Myers, E. L'Hopital, J.L. Provis, B. Lothenbach, Effect of temperature and aluminium on calcium (alumino)silicate hydrate chemistry under equilibrium conditions, Cem. Concr. Res. 68 (2015) 83–93.

[9] W.-S. Chiang, E. Fratini, P. Baglioni, D. Liu, S.-H. Chen, Microstructure determination of calcium-silicate-hydrate globules by small-angle neutron scattering, J. Phys. Chem. C 116 (2012) 5055–5061.

[10] M. Miller, C. Bobko, M. Vandamme, F.J. Ulm, Surface roughness criteria for cement paste nanoindentation, Cem. Concr. Res. 38 (2008) 467–476.

[11] P. Trtik, J. Dual, B. Muench, L. Holzer, Limitation in obtainable surface roughness of hardened cement paste: 'virtual' topographic experiment based on focussed ion beam nanotomography datasets, J. Microsc. Oxford 232 (2008) 200–206.

[12] G. Constantinides, K.S.R. Chandran, F.J. Ulm, K.J. Van Vliet, Grid indentation analysis of composite microstructure and mechanics: principles and validation, Mater. Sci. Eng. A Struct. 430 (2006) 189–202.

[13] W. Wilson, L. Sorelli, A. Tagnit-Hamou, Automated coupling of NanoIndentation and Quantitative Energy-Dispersive Spectroscopy (NI-QEDS): a comprehensive method to disclose the micro-chemo-mechanical properties of cement pastes, Cem. Concr. Res. 103 (2018) 49–65.

[14] O. Bernard, F.J. Ulm, E. Lemarchand, A multiscale mictomechanics-hydration model for the early-age elastic properties of cement-based materials, Cem. Concr. Res. 33 (2003) 1293–1309.

[15] P. Trtik, B. Munch, P. Lura, A critical examination of statistical nanoindentation on model materials and hardened cement pastes based on virtual experiments, Cement Concr. Comp. 31 (2009) 705–714.

[16] W. Wilson, Chemo-mechanical Characterization of Microstructure Phases in Cementitious Systems by a Novel NI-QEDS Technique, Université de Sherbrooke, 2017, p. 267.

[17] F. Pelisser, P.J.P. Gleize, A. Mikowski, Effect of the Ca/Si molar ratio on the micro/nanomechanical properties of synthetic C-S-H measured by nanoindentation, J. Phys. Chem. C 116 (2012) 17219–17227.

[18] F. Pelisser, P.J.P. Gleize, A. Mikowski, Structure and micro-nanomechanical characterization of synthetic calcium-silicate-hydrate with poly(vinyl alcohol), Cement Concr. Comp. 48 (2014) 1–8.

[19] W. Hunnicutt, P. Mondal, L. Struble, Dynamic and quasi-static nanoindentation of CSH and CASH, Special Publ. 312 (2016) 1–15.

[20] E.M. Foley, J.J. Kim, M.M.R. Taha, Synthesis and nano-mechanical characterization of calcium-silicate-hydrate (C-S-H) made with 1.5 CaO/SiO₂ mixture, Cem. Concr. Res. 42 (2012) 1225–1232.

[21] R. Hay, J. Li, K. Celik, Influencing factors on micromechanical properties of calcium (alumino) silicate hydrate C-(A-) SH under nanoindentation experiment, Cem. Concr. Res. 134 (2020) 106088.

[22] Z.L. Hu, M. Wyrzykowski, M. Griffa, K. Scrivener, P. Lura, Young's modulus and creep of calcium-silicate-hydrate compacts measured by microindentation, Cement Concr. Res. 134 (2020).

[23] G. Geng, R.J. Myers, J. Li, R. Maboudian, C. Carraro, D.A. Shapiro, P.J. Monteiro, Aluminum-induced dreierketten chain cross-links increase the mechanical properties of nanocrystalline calcium aluminosilicate hydrate, Sci. Rep. 7 (2017) 44032.

[24] G. Geng, R.J. Myers, M.J.A. Qomi, P.J.M. Monteiro, Densification of the interlayer spacing governs the nanomechanical properties of calcium-silicate-hydrate, Sci. Rep. 7 (2017) 10986.

[25] G. Constantinides, F.J. Ulm, The nanogranular nature of C-S-H, J. Mech. Phys. Solids 55 (2007) 64–90.

[26] L.B. Skinner, S.R. Chae, C.J. Benmore, H.R. Wenk, P.J.M. Monteiro, Nanostructure of calcium silicate hydrates in cements, Phys. Rev. Lett. 104 (2010) 195502.

[27] P.K. Mehta, P.J. Monteiro, Concrete Microstructure, Properties and Materials, McGraw-Hill, New York, 2017.

[28] L. Sorelli, G. Constantinides, F.-J. Ulm, F. Toutlemonde, The nano-mechanical signature of ultra high performance concrete by statistical nanoindentation techniques, Cem. Concr. Res. 38 (2008) 1447–1456.

[29] W. Zhu, J.J. Hughes, N. Bicanic, C.J. Pearce, Nanoindentation mapping of mechanical properties of cement paste and natural rocks, Mater. Charact. 58 (2007) 1189–1198.

[30] M. Sebastiani, R. Moscatelli, F. Ridi, P. Baglioni, F. Carassiti, High-resolution high-speed nanoindentation mapping of cement pastes: unravelling the effect of microstructure on the mechanical properties of hydrated phases, Mater. Des. 97 (2016) 372–380.

[31] C.L. Hu, Y.Y. Gao, Y.M. Zhang, Z.J. Li, Statistical nanoindentation technique in application to hardened cement pastes: influences of material microstructure and analysis method, Constr. Build. Mater. 113 (2016) 306–316.

[32] J.J. Hughes, P. Trtik, Micro-mechanical properties of cement paste measured by depth-sensing nanoindentation: a preliminary correlation of physical properties with phase type, Mater. Charact. 53 (2004) 223–231.

[33] H.M. Jennings, J.J. Thomas, J.S. Gevrenov, G. Constantinides, F.J. Ulm, A multi-technique investigation of the nanoporosity of cement paste, Cem. Concr. Res. 37 (2007) 329–336.

[34] G. Constantinides, F.J. Ulm, The effect of two types of C-S-H on the elasticity of cement-based materials: results from nanoindentation and micromechanical modeling, Cem. Concr. Res. 34 (2004) 67–80.

[35] G. Geng, R.N. Vasin, J. Li, M.J.A. Qomi, J. Yan, H.R. Wenk, P.J.M. Monteiro, Preferred orientation of calcium aluminosilicate hydrate induced by confined compression, Cem. Concr. Res. 113 (2018) 186–196.

[36] A. Morshedifard, S. Masoumi, M.J.A. Qomi, Nanoscale origins of creep in calcium silicate hydrates, Nat. Commun. 9 (2018) 1–10.

[37] C.E. White, N. Garg, D. Olds, J. Vocaturo, S.M. Everett, K. Page, A uniaxial load frame for in situ neutron studies of stress-induced changes in cementitious materials and related systems, Rev. Sci. Instrum. 89 (2018), 092903.

[38] M. Vandamme, F.J. Ulm, Nanogranular origin of concrete creep, P. Natl. Acad. Sci. U. S. A. 106 (2009) 10552–10557.

[39] Z.P. Bazant, A.B. Hauggaard, S. Baweja, F.J. Ulm, Microprestress-solidification theory for concrete creep. 1. Aging and drying effects, J. Eng. Mech. ASCE 123 (1997) 1188–1194.

[40] X.D. Li, Z.C. Grasley, J.W. Bullard, P. Feng, Creep and relaxation of cement paste caused by stress-induced dissolution of hydrated solid components, J. Am. Ceram. Soc. 101 (2018) 4237–4255.

[41] M. Wyrzykowski, K. Scrivener, P. Lura, Basic creep of cement paste at early age - the role of cement hydration, Cem. Concr. Res. 116 (2019) 191–201.

[42] P. Klug, F. Wittmann, Activation energy and activation volume of creep of hardened cement paste, Mater. Sci. Eng. 15 (1974) 63–66.

[43] J.J. Thomas, H.M. Jennings, A colloidal interpretation of chemical aging of the C-S-H gel and its effects on the properties of cement paste, Cem. Concr. Res. 36 (2006) 30–38.

[44] D.T. Nguyen, R. Alizadeh, J.J. Beaudoin, P. Pourbeik, L. Raki, Microindentation creep of monophasic calcium-silicate-hydrates, Cement Concr. Comp. 48 (2014) 118–126.

[45] M. Lopez, L.F. Kahn, K.E. Kurtis, Effect of internally stored water on creep of high-performance concrete, ACI Mater. J. 105 (2008) 265–273.

[46] B.T. Tamtsia, J.J. Beaudoin, Basic creep of hardened cement paste - a re-examination of the role of water, Cem. Concr. Res. 30 (2000) 1465–1475.

[47] K. Scrivener, R. Snellings, B. Lothenbach, A Practical Guide to Microstructural Analysis of Cementitious Materials, CRC Press, Boca Raton, 2016.

[48] J. Zhang, G.W. Scherer, Comparison of methods for arresting hydration of cement, Cem. Concr. Res. 41 (2011) 1024–1036.

[49] E. L'Hôpital, B. Lothenbach, K. Scrivener, D. Kulik, Alkali uptake in calcium alumina silicate hydrate (CASH), Cem. Concr. Res. 85 (2016) 122–136.

[50] F. Battocchio, P.J.M. Monteiro, H.R. Wenk, Rietveld refinement of the structures of 1.0 C-S-H and 1.5 C-S-H, Cem. Concr. Res. 42 (2012) 1534–1548.

[51] S. Merlino, E. Bonaccorsi, T. Armbruster, Tobermorites: their real structure and order-disorder (OD) character, Am. Mineral. 84 (1999) 1613–1621.

[52] S. Merlino, E. Bonaccorsi, T. Armbruster, The real structures of clinotobermorite and tobermorite 9 angstrom: OD character, polytypes, and structural relationships, Eur. J. Mineral. 12 (2000) 411–429.

[53] S. Merlino, E. Bonaccorsi, A.R. Kampf, Tobermorite 14 angstrom: crystal structure and OD character, Appl. Mineral. 1 and 2 (2000) 859–861.

[54] I.G. Richardson, Model structures for C-(A)-SH (I), Acta Crystallogr. Sect. B: Struct. Sci. Cryst. Eng. Mater. 70 (2014) 903–923.

[55] S. Merlino, E. Bonaccorsi, T. Armbruster, The real structure of tobermorite 11 angstrom: normal and anomalous forms, OD character and polytypic modifications, Eur. J. Miner. 13 (2001) 577–590.

[56] L. Lutterotti, R. Vasin, H.-R. Wenk, Rietveld texture analysis from synchrotron diffraction images. I. Calibration and basic analysis, Powder Diffract. 29 (2014) 76–84.

[57] H.-R. Wenk, L. Lutterotti, P. Kaercher, W. Kanitpanyacharoen, L. Miyagi, R. Vasin, Rietveld texture analysis from synchrotron diffraction images. II. Complex multiphase materials and diamond anvil cell experiments, Powder Diffract. 29 (2014) 220–232.

[58] I. Lonardelli, H.R. Wenk, Y. Ren, Preferred orientation and elastic anisotropy in shales, Geophysics 72 (2007) D33–D40.

[59] H.R. Wenk, I. Lonardelli, H. Franz, K. Nihei, S. Nakagawa, Preferred orientation and elastic anisotropy of illite-rich shale, Geophysics 72 (2007) E69–E75.

[60] H.M. Jennings, Refinements to colloid model of C-S-H in cement: CM-II, Cem. Concr. Res. 38 (2008) 275–289.

[61] H.-R. Wenk, P.J. Monteiro, M. Kunz, K. Chen, N. Tamura, L. Lutterotti, J. Del Arroz, Preferred orientation of ettringite in concrete fractures, J. Appl. Crystallogr. 42 (2009) 429–432.

[62] H.R. Wenk, Preferred Orientation in Deformed Metal and Rocks: An Introduction to Modern Texture Analysis, Elsevier, 2016.

[63] E. Kaminski, The influence of water on the development of lattice preferred orientation in olivine aggregates, Geophys. Res. Lett. 29 (2002) (17-11-17-14).

[64] H. Jung, S.-i. Karato, Water-induced fabric transitions in olivine, Science 293 (2001) 1460–1463.

[65] H.R. Wenk, P. Kaercher, W. Kanitpanyacharoen, E. Zepeda-Alarcon, Y. Wang, Orientation relations during the alpha-omega phase transition of zirconium: in situ texture observations at high pressure and temperature, Phys. Rev. Lett. 111 (2013).

[66] S. Masoumi, H. Valipour, M.J. Abdolhosseini Qomi, Interparticle interactions in colloidal systems: toward a comprehensive mesoscale model, ACS Appl. Mater. Interfaces 9 (2017) 27338–27349.

[67] J. Li, W. Zhang, P.J. Monteiro, Synchrotron X-ray Raman scattering shows the changes of the Ca environment in CSH exposed to high pressure, Cem. Concr. Res. 132 (2020) 106066.

[68] I. Pignatelli, A. Kumar, R. Alizadeh, Y. Le Pape, M. Bauchy, G. Sant, A dissolution-precipitation mechanism is at the origin of concrete creep in moist environments, J. Chem. Phys. 145 (2016), 054701.

[69] N. Ranaivomanana, S. Multon, A. Turatsinze, Tensile, compressive and flexural basic creep of concrete at different stress levels, Cem. Concr. Res. 52 (2013) 1–10.

[70] P. Rossi, J.L. Tailhan, F. Le Maou, Comparison of concrete creep in tension and in compression: influence of concrete age at loading and drying conditions, Cem. Concr. Res. 51 (2013) 78–84.

[71] R. Alizadeh, J.J. Beaudoin, L. Raki, Viscoelastic nature of calcium silicate hydrate, Cement Concr. Comp. 32 (2010) 369–376.

[72] R.F. Feldman, Mechanism of creep of hydrated Portland cement paste, Cem. Concr. Res. 2 (1972) 521–540.

[73] P. Suwanmaneechot, A. Aili, I. Maruyama, Creep behavior of CSH under different drying relative humidities: interpretation of microindentation tests and sorption measurements by multi-scale analysis, Cem. Concr. Res. 132 (2020) 106036.

[74] J. Li, W. Zhang, K. Garbev, G. Beuchle, P.J. Monteiro, Influences of cross-linking and Al incorporation on the intrinsic mechanical properties of tobermorite, Cem. Concr. Res. 136 (2020) 106170.

[75] J. Li, W. Zhang, P.J.M. Monteiro, The structure and intrinsic mechanical properties of nanocrystalline calcium silicate hydrate, ACS Sustain. Chem. Eng. 8 (2020) 12453–12461.

[76] J. Nemecek, Creep effects in nanoindentation of hydrated phases of cement pastes, Mater. Charact. 60 (2009) 1028–1034.

[77] J. Fu, S. Kamali-Bernard, F. Bernard, M. Cornen, Comparison of mechanical properties of C-S-H and portlandite between nano-indentation experiments and a modeling approach using various simulation techniques, Compos. Part B Eng. 151 (2018) 127–138.

[78] H. Bei, E.P. George, J. Hay, G.M. Pharr, Influence of indenter tip geometry on elastic deformation during nanoindentation, Phys. Rev. Lett. 95 (2005), 045501.

[79] P. Lura, P. Trtik, B. Munch, Validity of recent approaches for statistical nanoindentation of cement pastes, Cement Concr. Comp. 33 (2011) 457–465.

[80] Z. Chen, J. Frech-Baronet, L. Sorelli, A microindentation two-fold creep model for characterizing short-and long-term creep behavior of a cement paste, Mech. Mater. 150 (2020) 103559.

[81] J. Moon, S. Speziale, C. Meral, B. Kalkan, S.M. Clark, P.J. Monteiro, Determination of the elastic properties of amorphous materials: case study of alkali–silica reaction gel, Cem. Concr. Res. 54 (2013) 55–60.

[82] D.W. Gardner, J. Li, A. Morshedifard, S. Masoumi, M.J. Abdolhosseini Qomi, P. J. Monteiro, R. Maboudian, C. Carraro, Silicate bond characteristics in calcium-silicate-hydrates determined by high pressure Raman spectroscopy, J. Phys. Chem. C 124 (33) (2020) 18335–18345.

[83] H.F.W. Taylor, Cement Chemistry, Thomas Telford, 1997.

[84] S. Bae, C. Meral, J.-e. Oh, J. Moon, M. Kunz, P.J. Monteiro, Characterization of morphology and hydration products of high-volume fly ash paste by monochromatic scanning X-ray micro-diffraction (μ-SXRD), Cem. Concr. Res. 59 (2014) 155–164.

[85] A. Palomo, P. Monteiro, P. Martauz, V. Bilek, A. Fernandez-Jimenez, Hybrid binders: a journey from the past to a sustainable future (opus caementicium futurum), Cem. Concr. Res. 124 (2019) 105829.

[86] W. Wilson, J.M. Rivera-Torres, L. Sorelli, A. Duran-Herrera, A. Tagnit-Hamou, The micromechanical signature of high-volume natural pozzolan concrete by combined statistical nanoindentation and SEM-EDS analyses, Cem. Concr. Res. 91 (2017) 1–12.